



Research Article

Annealing effects on structural and photovoltaic properties of the dip-SILAR-prepared bismuth oxyhalides (BiOI, Bi₇O₉I₃, Bi₅O₇I) films

R. MD Matiur¹  · A. A. Abuelwafa^{1,2} · Anissa A. Putri³ · S. Kato¹ · N. Kishi¹ · T. Soga¹

Received: 22 October 2020 / Accepted: 4 January 2021 / Published online: 15 January 2021
© The Author(s) 2021 

Abstract

Bismuth oxyhalides are becoming a promising contender for photovoltaic applications due to its non-toxic nature and decent optical properties. This study mainly deals with clarifying the effects of phase transformations on the structure, optical, and electrical properties of BiOI thin film prepared via dip-successive ionic layer adsorption and reaction (SILAR) method at different annealing temperatures ranging from 100 to 400 °C. Therefore, significant phase transformations (i.e., the existence of Bi₇O₉I₃ and Bi₅O₇I have been confirmed at 300 °C and 400 °C, respectively) appeared in the produced films, which were mainly due to the change of annealing temperatures. The experimental results confirmed that produced films achieved the maximum current density and efficiency and minimum current density and efficiency at 100 °C and 400 °C, respectively. Experimental results were also showed that with increasing the annealing temperature from 100 to 400 °C, the indirect bandgap risen from 1.77 to 2.96 eV while the crystallite size decreased from 17.62 to 12.99 nm. The energy band diagram with electrolyte explained the observed poor electrical properties during the phase transformation. Hence, this result will add positive impacts on the new information on findings for the dip-SILAR-prepared BiOI photovoltaic cells.

Keywords Phase transformation · Bismuth oxyiodide · Dip-SILAR · Structure · Electrical properties

1 Introduction

Bismuth oxyiodides (BiOI) is being used as a photocatalyst for the photocatalytic reaction since its first discovery [1–9]. Besides, BiOI is a p-type material, and the decent band-gap, environment-friendly properties make this broader adaption into different applications [10]. Moreover, because of the higher stability, high tolerance in defect, and inexpensive nature of the BiOI, the researcher was attracted to consider and develop it as a photoanode for the photo-electrochemical devices [11–17]. Addressing the necessity of a stable BiOI material research world is trying various synthesis

techniques for the production of BiOI with the help of various solvents [5, 11, 16, 18–20]. The solvothermal and hydrothermal methods are commonly known to synthesize the BiOI powder for photocatalytic applications [9, 18, 19]. Besides that, the doctor blade and chemical-based deposition techniques have been widely used to deposit BiOI films for photovoltaic studies [13, 14, 16, 21]. All the previous research shows that the synthesis technique impacts the morphology and structure of the BiOI material, which eventually affects the device performance. Therefore, in our experiment the BiOI thin film's deposition has been conducted via dip-successive ionic layer adsorption and reaction (SILAR) technique.

✉ R. MD Matiur, md.matiurrahman20@gmail.com | ¹Department of Electrical and Mechanical Engineering, Nagoya Institute of Technology, Gokiso-cho, Showa-ku, Nagoya 466-8555, Japan. ²Nano & Thin Film Lab. Physics Department, Faculty of Science, South Valley University, Qena 83523, Egypt. ³Department of Chemistry, Walisongo State Islamic University, Semarang 50185, Indonesia.



Furthermore, morphology, crystallite size, and optical properties can be substantially affected if the film development process changes, such as the change of concentration of the raw material [21–24], selection of surfactant, and solvent selection [25, 26]. After the deposition process, post-treatment, such annealing temperature can also significantly affect the material properties [21]. In progress, some studies show that the annealing treatment helps to get the derivatives of the BiOI materials, which causes some remarkable improvement in the photocatalytic performance [27]. As a result, the derivatives of BiOI are the most attractive and favorably reported materials in photocatalytic applications.

Another comparative study confirmed that for photocatalyst activity, $\text{Bi}_4\text{O}_5\text{I}_2$ is better than BiOI. This is because smaller size and broader valance band reduce the electron-hole pair recombination rate [21, 28, 29]. Furthermore, BiOI and one of its derivatives, i.e., $\text{Bi}_7\text{O}_9\text{I}_3$, showed the same properties reported for photocatalytic purposes, mostly under visible light irradiation [27, 30]. On the other hand, from $\text{Bi}_5\text{O}_7\text{I}$, the photocatalytic activity was found two times better than that of BiOI because the pore size and band structure were played a vital role [31]. However, so far, there is no reported research article to check the post-annealing treatment on the dip-SILAR prepared BiOI/FTO thin film's morphology, structure, optical and photovoltaic properties. Therefore, this study aims to prepare dip-SILAR BiOI thin films on glass substrate with an improved photovoltaic performance at different annealing temperatures. The purpose of this paper is to investigate the phase transformation effect on the structure, morphology, optical, and photovoltaic properties of BiOI thin films grown by dip-SILAR method.

2 Materials and methodology

2.1 Materials

In our experiment, 2 cm × 2 cm fluorine-doped tin oxide (FTO) glass was used as a substrate. For cleaning the FTO glass substrate, we used acetone, ethanol, and N_2 gas, respectively. Moreover, during the experimental process, $\text{Bi}(\text{NO}_3)_3 \cdot 5\text{H}_2\text{O}$ and KI (Purchased from Nacalai Tesque, Inc. Kyoto, Japan) was used as a cation and anion source, respectively. All solvents were used without further purification. Ultrapure water was collected from Milli-Q direct water purification system (resistivity: 18.2 M Ω -cm and temperature: 25 °C).

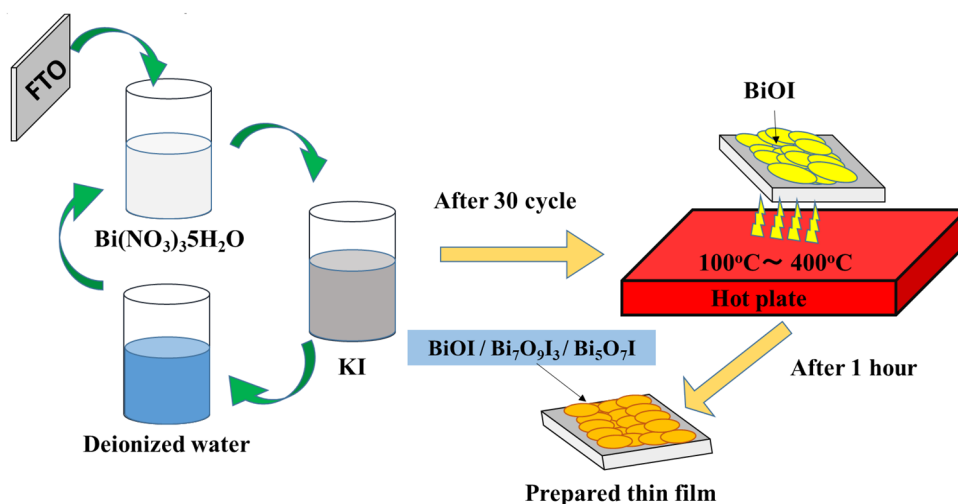
2.2 Experimental methodology

BiOI thin films were deposited on the top of cleaned FTO (2 cm × 2 cm) substrate via the dip-SILAR process. For the deposition purpose, 6 mM concentrated $\text{Bi}(\text{NO}_3)_3 \cdot 5\text{H}_2\text{O}$ (pH value: 2.1) and KI solution (pH value: 4.8) were prepared, respectively. After that, the FTO initially dipped into the $\text{Bi}(\text{NO}_3)_3 \cdot 5\text{H}_2\text{O}$, followed by dipping into the KI solution. Hereafter, once cleaned with deionized water to complete one SILAR cycle. The substrate was dipped into each solution for 20 s, and the dip-SILAR process continued for up to 30 cycles. Finally, the films' in the presence of air were annealed within the temperature range of 100–400 °C for 1 h. The flow of the experiment is shown in Fig. 1.

2.3 Characterizations

The structural characterizations were performed using the XRD instrument (Rigaku Smartlab, XRD). The Raman shift of the thin films was detected by the Raman

Fig. 1 Illustration of the preparation of BiOI and its derivative composites on FTO



spectroscopy (JASCO NRS-1500W) under room temperature condition with excitation wavelength of 532 nm. The prepared samples' morphology was heeded by using a scanning electron microscopy (SEM, JSM-6510). The energy dispersive X-ray spectrometer (EDS) was performed using field emission scanning electron microscope (JEOL: JSM-7001FF) to evaluate the composition of the films. The transmittance $T(\lambda)$ and reflectance $R(\lambda)$ were recorded to analyze the optical properties at normal incidence in the wavelength range of 300–1500 nm using the UV-Visible NIR spectroscopy (JASCO 670 UV).

2.4 Fabrication of electrochemical cell and photovoltaic application

After the dip-SILAR process and different annealing temperature treatments, samples were prepared to employ in the photovoltaic cell in our study. Finally, to prepare the complete solar cell, we used a counter electrode (Pt-coated glass), which was attached to a polymer film (Himilan, 50 μm). Again, in between the BiOI film and counter electrode, I^-/I_3^- redox (Solaronix Iodolyte AN-50) was used as an electrolyte. So, our complete cell structure was composed of FTO/BiOI/Iodine electrolyte/Pt-FTO/glass (Fig. 2). To record photo-current–voltage (I–V), a solar simulator (100 mW/cm^2 , AM 1.5 illumination) was used, where the light illumination active area dimension was 0.16 cm^2 .

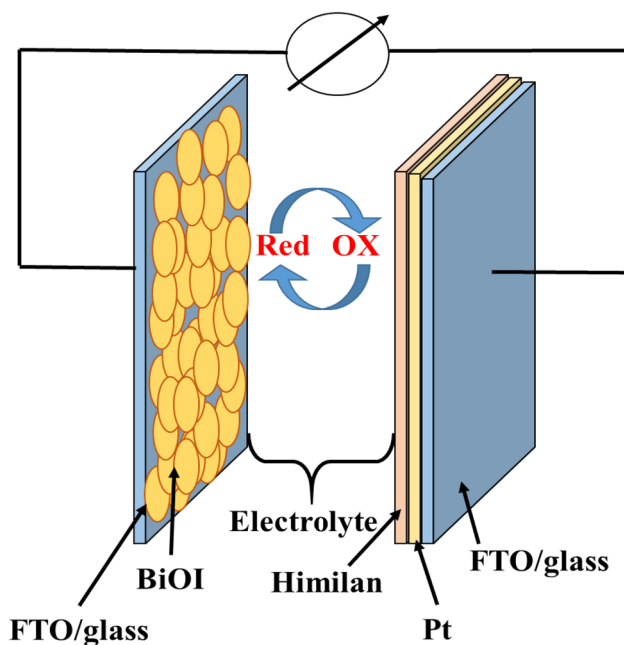


Fig. 2 Illustration of BiOI/FTO glass substrate photovoltaic device structure

3 Results and discussion

3.1 Structural properties

3.1.1 X-ray diffraction analysis

BiOI material was deposited at different annealing temperatures on top of the FTO glass substrate, and the change of X-ray diffraction patterns was observed (Fig. 3a). The sample prepared at without annealing condition (i.e., at 25 $^{\circ}\text{C}$), the XRD pattern shows the (002), (102), (110), and (200) planes at 19.3 $^{\circ}$, 29.7 $^{\circ}$, 31.7 $^{\circ}$, and 45.5 $^{\circ}$, which is matched with the Joint Committee on Powder Diffraction Standards (JCPDS) card of BiOI No. 00-73-2062. Whenever the BiOI/FTO glass substrate film was annealed at 100 $^{\circ}\text{C}$, the peaks' sharpness is increased at 19.3 $^{\circ}$, 29.7 $^{\circ}$, 31.7 $^{\circ}$, and 45.5 $^{\circ}$, which is the indication of the bigger crystallite size. The present authors have reported that 100 $^{\circ}\text{C}$ is the optimal temperature for obtaining better uniform film, and under this temperature, BiOI reaches its good physical structure [32]. Again, further increase of annealing temperature means at 200 $^{\circ}\text{C}$, the full width at half maximum (FWHM) becomes broader. The peak increased at 19.3 $^{\circ}$ disappeared, and other three peaks are the same as the 100 $^{\circ}\text{C}$, but the changes happen in the intensity and reduction of peak sharpness. In the XRD pattern, the reduction of the peak sharpness indicates the smaller crystallite size. Moreover, the increasing annealing temperature causes desorption of iodine resulting in the increase of defect density, which will be discussed later, but until

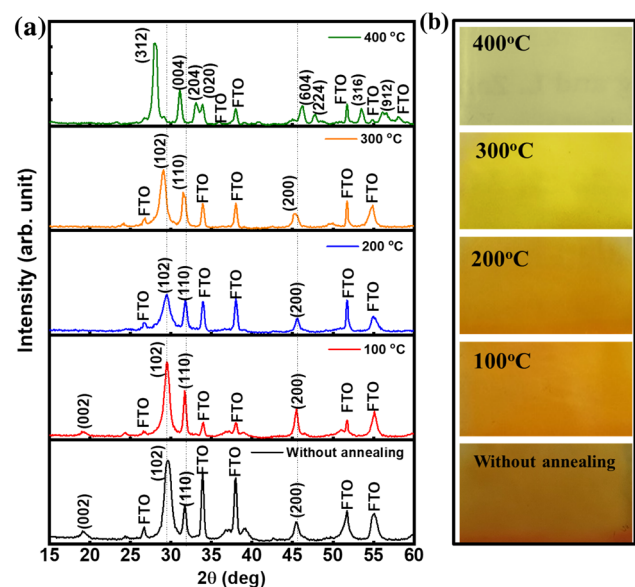
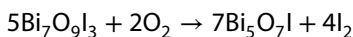
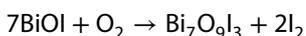


Fig. 3 **a** XRD pattern of BiOI/FTO thin films and **b** Digital photographs of the prepared samples at various annealing temperature

200 °C BiOI belongs to its own characteristics [33, 34]. As a consequence of that, change has been observed in the XRD pattern. If we compare the 100 °C and 200 °C annealing temperature, the plane (102) at 300 °C annealing temperature shifted towards the smaller 2θ. The reason is that more bismuth and oxygen are contained in the BiOI lattice crystal [21]. Here, the peak at 31.59° has a d-spacing 0.283 nm, that is identical with the JCPDS card no 00-04-0548 and 38-0669. Again, some research articles reported that 0.286 nm is the d-spacing for Bi₇O₉I₃ [21]. So, we can say that the peak we got at 300 °C annealing temperature is for the Bi₇O₉I₃ phase. Moreover, some literatures are calming identical planes for Bi₇O₉I₃ phase as BiOI [35].

Again, according to the JCPDS card No. 00-40-0548, Bi₅O₇I crystal planes (001), (312), (004), (204), (020), and (316) were found at around 7.7°, 28.2°, 31.09°, 33.02°, 33.4°, and 53.6°. Moreover, JCPDS card No. 380669 also confirms that it found the Bi₅O₇I crystal planes at 28.08°, 31.08°, 33.02°, 56.08°, 56.67°. In our study, at 400 °C annealing temperature, we found the peaks at the same line. The more structural details of Bi₅O₇I can be found in some previous studies [36]. The phase transformation reactions at 300 °C and 400 °C are expressed as follows, respectively.



In the texture of materials, the preferred orientation is the most favorable direction, which arises because the material has a strong tendency to crystallize in a specific direction. The preferred orientation can be determined by the highest value of the texture coefficient (TC) [37, 38]. Moreover, if the value of TC equals 1, that indicates the crystallites will be randomly oriented. However, if TC > 1, then the crystallites will be oriented in a particular (hkl) direction. Meanwhile, the higher the value of TC, the

greater the number of crystallites which are periodically oriented. In our study for 100 °C, the annealing film TC value has been calculated (see Table 1) according to the literature [37, 38]. Among, all the diffraction plan, the largest intensity (TC = 1.55) has been observed for (102). So, diffraction plane (102) is the most favorable.

Again, let's look at Fig. 3b; it is quite clear that as the annealing temperature increases, the color of the film also changes, which is also the indication of the phase transformation. Here, at 100 °C and 200 °C annealing temperature, the film's color doesn't vary that much, but when the annealing temperature goes to 300 °C the film color becomes yellowish. Meanwhile, at 400 °C, the BiOI/FTO film's annealing temperature color converts light yellowish. With the increasing of annealing temperature, the average crystallite size changes have also been observed. It is essential to check with the increasing annealing temperature how the crystallinity and the defects of the BiOI films change. The average crystallite size D, dislocation density δ, the number of crystallites, N_c, and the micro-strain ε_s are microstructural parameters that give us a clear idea about the microstructure of BiOI films. By using the same Scherrer's formula and reported equation [36, 39–41], we have calculated the structural parameters. All calculated values of D, δ, ε_s, and N_c under different annealing temperatures are included in Table 2. The crystallite size increases with the annealing at 100 °C, then decreasing from 17.62 to 12.99 nm as the annealing temperature changes from 100 to 400 °C. However, dislocation density decreases at 100 °C and increases from 0.32 × 10¹⁶ to 0.59 × 10¹⁶ m⁻², which means the length of the dislocation lines per unit increases with the increasing annealing temperature volume is increased.

On the other hand, the microstrain and the number of crystallite values were increased. Moreover, with the increase of annealing temperature, more point defects were increased in the films, and the crystallite size reduction caused an increase in the grain boundaries. The BiOI/FTO films' images under different annealing temperatures were attached beside XRD patterns in Fig. 3b. At the 100 °C temperature, the color of the film is deep orange, and as the temperature started to increase, the color of the BiOI film started to become yellowish, and at 400 °C it became

Table 1 Texture coefficient values (TC) of major lines: BiOI (100 °C)

Diffraction plane	TC
(102)	1.55
(110)	0.94
(200)	0.58

Table 2 The Structural parameters for the BiOI/FTO thin films at varied annealing temperature

Annealing temperature (°C)	D(nm)	(δ × 10 ¹⁶) (m ⁻²)	N _c (m ⁻²) × 10 ¹⁷	ε _s × 10 ⁻³
Without annealing	15.55	0.41	1.02	2.34
100	17.62	0.32	0.91	2.14
200	14.70	0.46	1.57	2.73
300	13.24	0.57	2.16	2.78
400	12.99	0.59	2.28	2.90

light yellowish. The variation in color change occurs due to the phase transformation of the BiOI.

3.1.2 Raman spectroscopy analysis

We did the Raman spectroscopy analysis to examine other structural studies of the dip-SILAR-prepared BiOI/FTO glass substrate films (Fig. 4). Here, for without annealing prepared BiOI/FTO film, we got a small peak in Raman spectra at 149.6 cm^{-1} , which is matching with the reported study

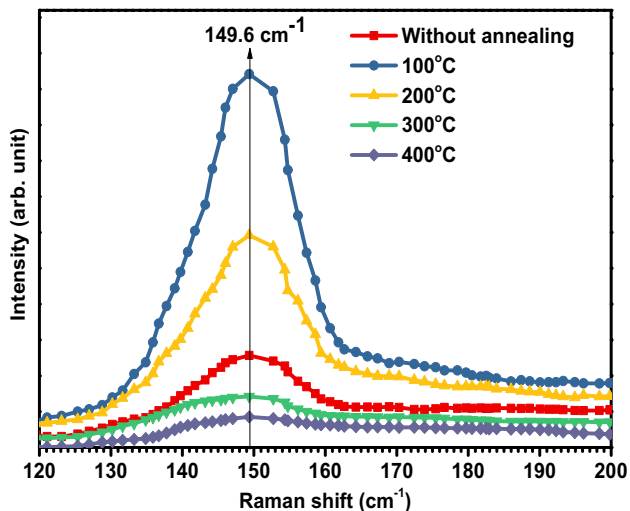


Fig. 4 Raman spectra of the for the BiOI/ FTO thin films at different annealing temperature

of BiOI [15, 21, 42, 43]. Again, after depositing BiOI, when the film is annealed at $100\text{ }^{\circ}\text{C}$ for 1 h, we got the high-intensity peak in Raman spectra at 149.6 cm^{-1} position. At $200\text{ }^{\circ}\text{C}$ annealing temperature condition, the prepared sample is also showing the peak at the same position as like as $100\text{ }^{\circ}\text{C}$ and without annealing condition, but the peak intensity is higher than the without annealing and lower than the $100\text{ }^{\circ}\text{C}$ temperature.

When the annealing temperature increased to $300\text{ }^{\circ}\text{C}$, in Raman spectra, there is a broader peak at the 149.6 cm^{-1} positions. That is maybe because of the phase transformation of the BiOI materials. Again, at $400\text{ }^{\circ}\text{C}$ seems like there is a broader peak in the region of the $120\text{--}200\text{ cm}^{-1}$. Because of phase transformation ($\text{Bi}_5\text{O}_7\text{I}$) and at the higher temperature, the vibration mode of the Bi-I shifted towards the higher frequency. Another reason as our sample changes to FTO color that is why we maybe we didn't get any peak at $400\text{ }^{\circ}\text{C}$. Moreover, some Raman study of $\text{Bi}_5\text{O}_7\text{I}$ material confirmed that they got a peak at the range of $200\text{--}360\text{ cm}^{-1}$ and $520\text{--}600\text{ cm}^{-1}$ [21].

3.1.3 Study of morphology

Figure 5 shows how the change of annealing temperature affects the BiOI/FTO thin films' morphology growth. In Fig. 5a, the morphology at without annealing condition is showing that a decent amount of small size flakes is generated. At $100\text{ }^{\circ}\text{C}$ annealing temperature in the morphological view (Fig. 5b), a decent number of flakes are generated. Some more bright flakes are visible (Fig. 5b) because of the

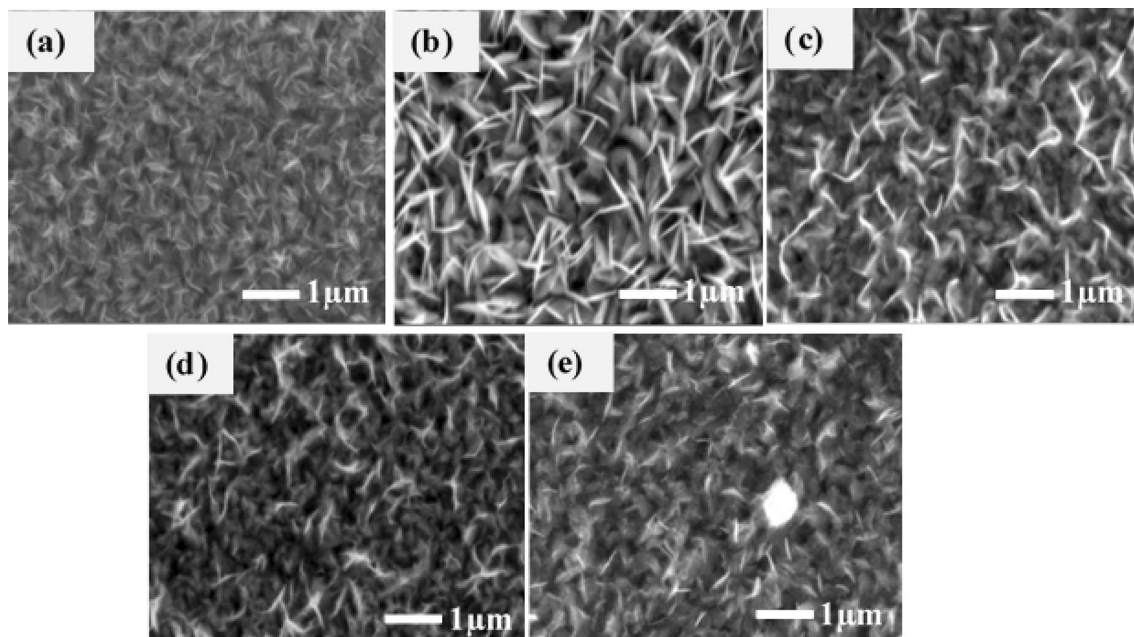


Fig. 5 SEM image for BiOI/FTO films: Annealing Temperature: **a** without annealing **b** $100\text{ }^{\circ}\text{C}$ **c** $200\text{ }^{\circ}\text{C}$ **d** $300\text{ }^{\circ}\text{C}$ **e** $400\text{ }^{\circ}\text{C}$

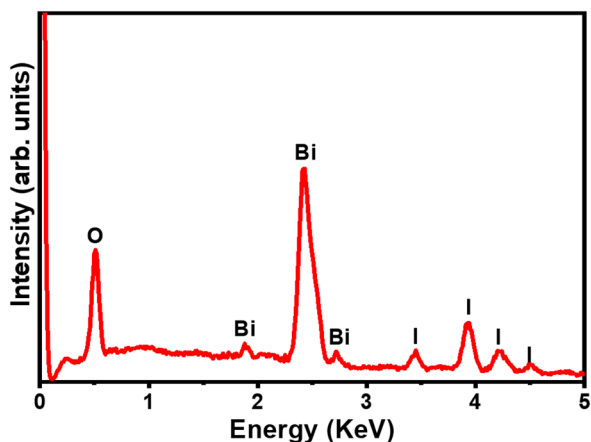
increase of the flake’s diameter. Again, all the flakes are connected to each other. When the annealing temperature increased from 100 to 200 °C, that time number of flakes and the connection between the flakes were also started to decrease (Fig. 5c). Furthermore, if we see Fig. 5d, at 300 °C annealing temperature, the flakes number and diameter were decreased compared to the 200 °C annealing temperature. Moreover, Fig. 5d shows that the connection between the flakes furthermore decreases. Finally, at 400 °C annealing temperature, very few percentages of the flakes are there. Meanwhile, a part of the FTO is visible (Fig. 5e), and there is no connection between the flakes, which is also partially agreeing with some previous study though that is not flakey growth. But in that study at the higher temperature, distortion of BiOI materials and the FTO visibility have been observed [44, 45].

3.2 EDS and thickness effect analysis

The annealing treatment causes a change in the film quality and structure of material. In our study to confirm the film quality and change in atomic concentration the energy dispersive X-ray spectrometer (EDS) has been performed and represented in Fig. 6. Figure 6 shows the EDS spectrum for 100 °C annealed film the atomic concentration of the Bi/I/O are 24%, 24%, 52% respectively. But as the annealing increased up to 200 °C, then atomic concentration of I is almost same. This is matching with the XRD result that film is BiOI up to 200 °C, then changes

to Bi₇O₉I₃ (300 °C) and then Bi₅O₇I (400 °C). However, the atomic concentration of I decreased to 20%. Here, for the BiOI material (at 100 °C) the Bi/I ratio is ~ 1 but for Bi₇O₉I₃ material (at 300 °C) the ratio increased ~ 1.4. Whenever, BiOI transformed into the Bi₅O₇I at 400 °C annealing temperature the ratio of Bi/I became 13.3. The increase of the Bi/I ratio and atomic concentration of O (%) actually introducing the defects in the film [32]. So, according to our study we can say that 100 °C annealing film is the most uniform film therefore there is a possibility to get decent electrical properties under this condition. Moreover, from the SEM picture the porosity percentage (Via ImageJ software) has been checked that is also showing lowest porosity percentage for the BiOI film which is annealed at 100 °C (see Fig. 7)

On the other hand, the percentage weight loss effects the thickness of the film. In our study till 100 °C the thickness increased and then started to decrease which is also showing an agreement with EDS analysis. Annealing temperature changes the physical properties of the material and our study also confirmed that till 100 °C the crystallite size increases. This increase of the crystallite size produces a better flakes connection, uniformity and film thickness. After 100 °C the BiOI material started losing weight which reduces the crystallite size, uniformity and thickness. Our prepared BiOI/FTO films’ measured thicknesses are without annealing: 482 nm, 100 °C: 507 nm, 200 °C: 493 nm, 300 °C: 235 nm, and 400 °C: 157 nm, respectively. Moreover, thickness is the utmost important parameter to tune optical and electrical properties. In our previous of optical characterization of the BiOI/FTO thin under different thickness also confirmed that around 500 nm is the optimal thickness for reaching decent optical properties [32].



Temperature	Bi (%)	I (%)	O (%)
100 ° C	~24	~24	~52
200 ° C	~24	~23.8	~52.2
300 ° C	~27	~20	~53
400 ° C	~32	~2.4	~66

Fig. 6 Typical EDS spectrum of 100 °C annealed BiOI and atomic composition at different annealing temperature

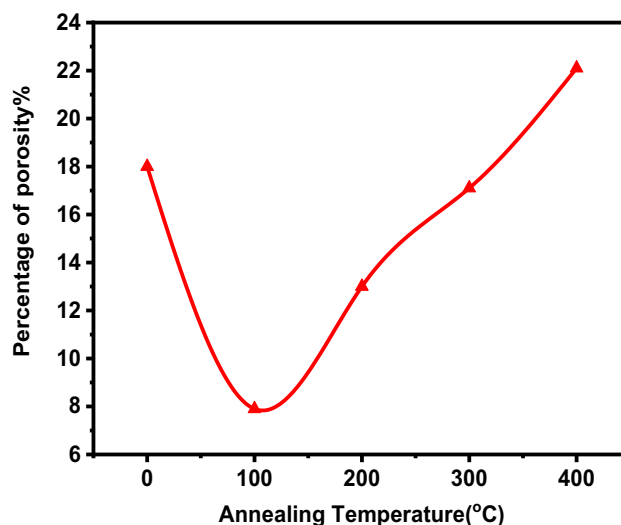


Fig. 7 Percentage porosity of BiOI/FTO thin film at different annealing temperature

3.3 Optical properties of BiOI

In solar cell performance the optical properties is very essential element because with the help of optical properties we can evaluate the potentially of the photovoltaic device [46, 47]. Herein, for our SILAR prepared BiOI/FTO thin films transmittance $T(\lambda)$ and reflectance $R(\lambda)$ has been recorded (wavelength range: 300–1500 nm) and represented in Fig. 8. In Fig. 8 if we see transmittance ($T(\lambda)$) spectra at the region of 300–600 nm the increasing edge shifting towards the shorter wavelength region. At 400 °C temperature annealed film shows the maximum transmittance throughout the 300–1500 nm wavelength region. This is just because of lower flakes connection and thickness reduction with annealing treatment. Moreover, in the reflectance spectrum in the range of 300–600 nm wavelength highest peak has been observed under 400 °C annealing condition. Hence, the higher transmittance and reflectance will cause the change in absorbance which also confirmed by absorbance measurement (see Fig. 9a).

Again, due to the temperature effect, the grain size and phase were changed; hence the absorbance was also affected. The absorption coefficient depends on the $T(\lambda)$ and $R(\lambda)$ [48]. Besides, by using the Tauc's relation showed in Eq. 1, the optical band-gap E_g^{Opt} have also been calculated (Fig. 9b). The details of can be found in literatures [49–52].

$$\alpha h\nu = A(h\nu - E_g^{Opt})^r \quad (1)$$

where, α is a parameter that depends on the transition probability, where h is Planck constant, ν is the frequency, and E_g^{Opt} is the optical band gap, and r is a number which describes the transition process ($r = 1/2$ in this work). The calculated values of the E_g^{Opt} were 1.77 eV for without annealing condition, 1.72 eV for 100 °C, 1.82 eV for 200 °C, 1.95 eV for 300 °C and 2.96 eV for 400 °C, respectively (see Fig. 9b). The optical band gaps of the BiOI films are almost constant up to 200 °C, then were increased with the annealing temperature. Here, the annealing temperature causes the change in flakes size (see Fig. 5), thickness, crystal phase, and the crystallite size (Table 2), etc. All these change is effecting the optical band-gap of BiOI material. Especially, the optical band-gap is changed by the quantum effect of nanocrystals. The slight increase from 1.77 eV (100 °C) to 1.82 eV (200 °C) would be due to the effect of quantum confinement that cause the reduction of the crystal size. The increasing flakes and crystallite size are reducing band-gap. On the other hand disappearance of the flakes, decrease of flakes and crystallite size causes the reduction of the optical band-gap. The details has been discussed in our previous study [32, 33]. Figure 3 shows that the crystal phase up 200 °C is BiOI, that at 300 °C is $\text{Bi}_7\text{O}_9\text{I}_3$, and that at 400 °C is $\text{Bi}_5\text{O}_7\text{I}$. Figure 3

Fig. 8 Transmittance $T(\lambda)$ and Reflectance $R(\lambda)$ of BiOI/FTO: Annealing Temperature: **a** without annealing **b** 100 °C **c** 200 °C **d** 300 °C **e** 400 °C

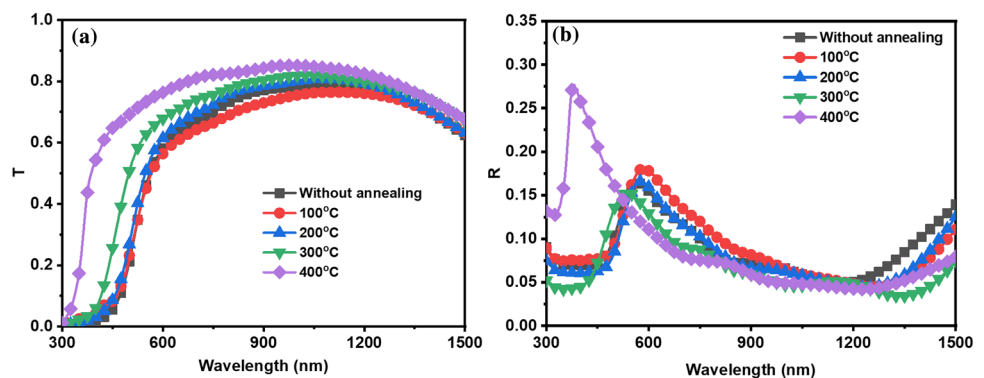
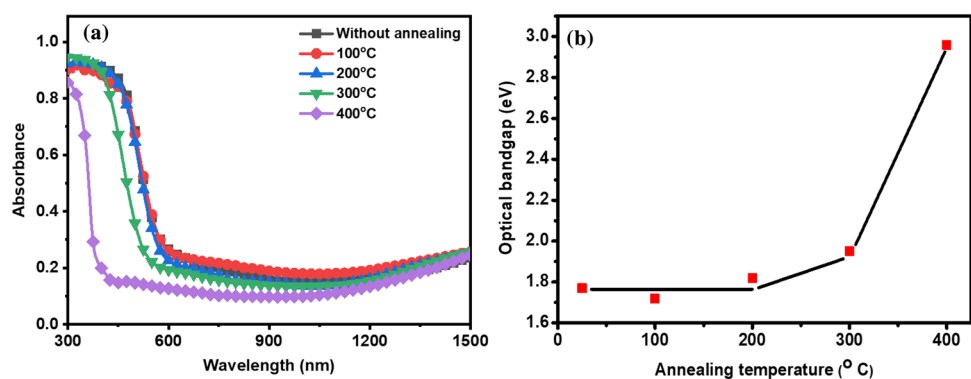


Fig. 9 Absorbance and Optical bandgap for different crystal phase (at different annealing temperature)



shows that the crystal phase up to 200 °C is BiOI, that at 300 °C is Bi₇O₉I₃, and that at 400 °C is Bi₅O₇I. The respective optical band-gap energies are around 1.77 eV, 1.95 eV, and 2.96 eV, matching with the literature [21, 53–55]. The previous study of the annealing effect for different preparation techniques was also showed that the band-gaps

were changed from 1.76 to 2.11 eV when the temperature changed from 100 to 550 °C [21, 44, 45].

3.4 Photovoltaic properties and energy diagram

The photovoltaic characterization has been represented in Figs. 10 and 11. Where, Fig. 10 denotes the I–V relationship and in Fig. 11, short circuit current density (J_{sc}), open-circuit voltage (V_{oc}), fill factor (FF), and power conversion efficiency (PCE) is plotted with respect to temperature for the prepared BiOI photovoltaic cells to make the optimal condition understandable. The study result shows that without annealing prepared cell reaches the $J_{sc} = 0.42 \text{ mA/cm}^2$, $V_{oc} = 0.38 \text{ V}$, and PCE = 0.05% value respectively. But when the prepared sample annealed at 100 °C for 1 h J_{sc} , V_{oc} and PCE improved by 1.5 times, 1.1 times, and 2.2 times respectively. Hence, at 100 °C annealing condition the value becomes $J_{sc} = 0.61 \text{ mA/cm}^2$, and $V_{oc} = 0.43 \text{ V}$, and PCE = 0.11%, (see Fig. 11). This improvement happens because with the increase of annealing temperature until 100 °C, the large crystallite size (see Table 2) and connection between the flakes increased (Fig. 5b), which may reduce the series resistance and improve effective surface area. Moreover, for electrochemical solar cells, a uniform flaky structure improves the effective surface area. That is why at 100 °C temperature conditions, maximum electrical

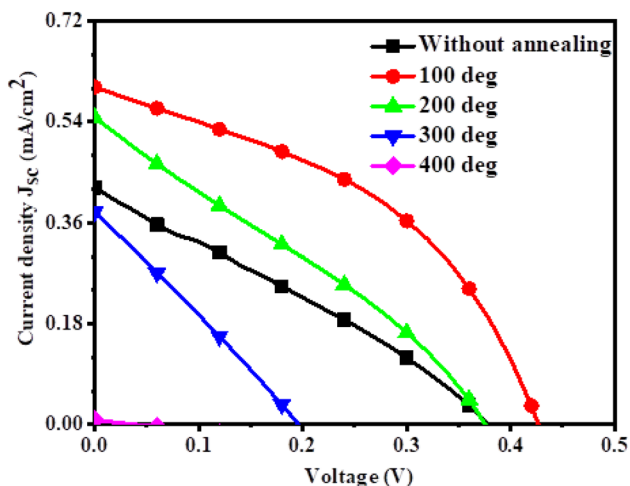
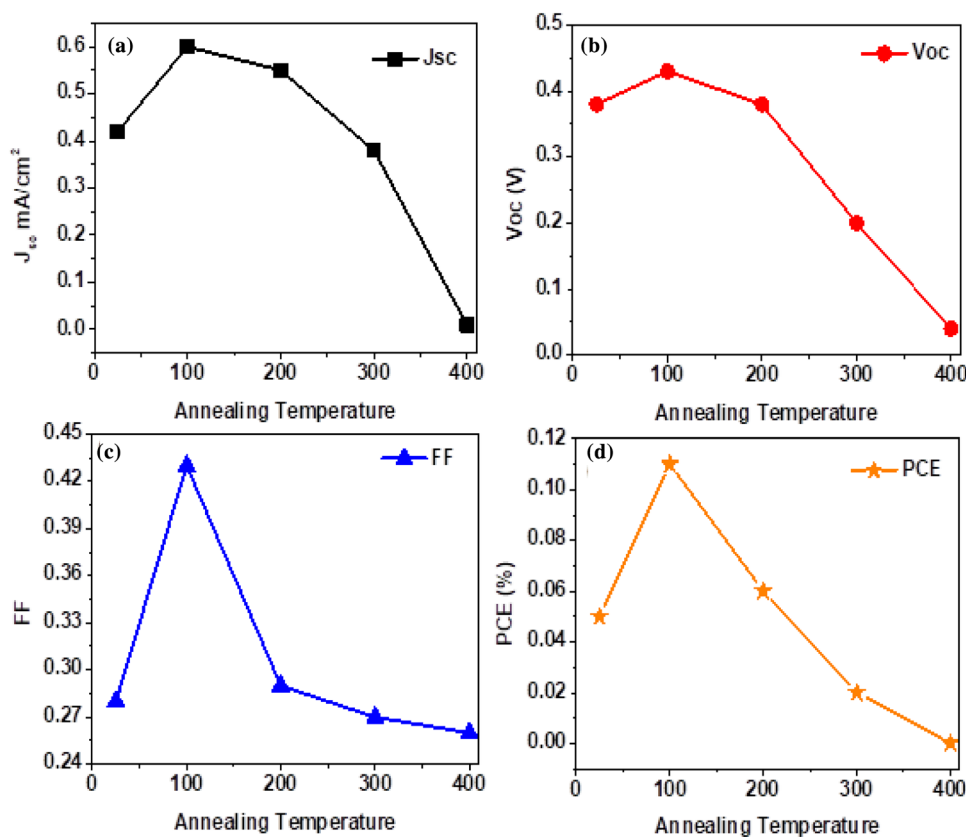


Fig. 10 Relationship between current-density and voltage between at different annealing temperature for dip-SILAR-prepared BiOI thin film based photovoltaic cell

Fig. 11 Performance of the dip-SILAR-prepared BiOI thin films in photovoltaic device: **a** short-circuit current density (J_{sc} (mA/cm²)) **b** open-circuit voltage (V_{oc} (V)) **c** fill factor (FF) **d** power conversion efficiency (PCE (%)) at various annealing temperatures



properties have been observed. However, with the further increase of the annealing temperature, the electrical properties decrease and almost reaches zero at 400 °C annealing temperature conditions. In cause of BiOI thin film, the increasing annealing temperature beyond 100 °C, the percentage weight loss started to increase [33], which causes the decrease in the crystallite size and introduces higher dislocation density (see Table 2). The SEM picture shows that after 100 °C, the flakes connection between the bright flakes started to decrease, which produced roughness and increased series resistance. Therefore, from 200 °C temperature, electrical properties started to decrease (see Fig. 11).

On the other hand, the variation of photovoltaic properties can also be explained by the energy band diagram. As displayed in Fig. 1, prepared bismuth oxyhalides are BiOI up to 200 °C annealing temperature, then above 300 °C annealing BiOI changes to $\text{Bi}_7\text{O}_9\text{I}_3$ (300 °C) and $\text{Bi}_5\text{O}_7\text{I}$ (400 °C). It is well-known that BiOI is a p-type semiconductor, whereas the Fermi level goes towards the vacuum level for $\text{Bi}_7\text{O}_9\text{I}_3$ and $\text{Bi}_5\text{O}_7\text{I}$ [51–53]. The energy band diagram for BiOI, $\text{Bi}_7\text{O}_9\text{I}_3$, and $\text{Bi}_5\text{O}_7\text{I}$ are shown theoretically in Fig. 12a, b, and c, respectively. Therefore, after the cell preparation the energy band diagram with the contact of I^-/I_3^- electrolyte can be illustrated as Fig. 12d, e, and f respectively. From the illustration, it is very clear that the increasing

energy gap and shifting of Fermi level reduce the carrier flow. As a result, the rising annealing temperature causes a decrease in current density. The short-circuit current also decreases with the annealing temperature because the created electron-hole pairs are decreased due to the large band-gap energy. The disappearance of the flaky structure and decrease of coverage is also the reason for the degradation of photovoltaic properties at 300 °C and 400 °C. Hereafter, the open-circuit voltage has a proportional relationship with the diffusion potential; if we look at the diffusion potential (V_{dp}) in Fig. 12d, e and f, it is started to decrease as the BiOI transformed into $\text{Bi}_7\text{O}_9\text{I}_3$, and $\text{Bi}_5\text{O}_7\text{I}$ respectively. That is in good agreement that open-circuit voltage decreases with the annealing temperature.

A previous study doctor blade method prepared BiOI solar cell has shown the maximum J_{sc} , V_{oc} , and efficiency 0.43 mA/cm², 0.44 V, and 0.06% respectively at 300 °C annealing temperature condition [21]. However, in our investigation for dip-SILAR-prepared BiOI/FTO photovoltaic cells, electrical properties are getting worse after the phase transformation. The maximum J_{sc} , V_{oc} , and efficiency are 0.61 mA/cm², 0.43 V, and 0.11%, respectively at 100 °C annealing temperature. We believe that this study result will add some valuable information for the dip-SILAR-prepared BiOI/FTO glass substrate photovoltaic cell.

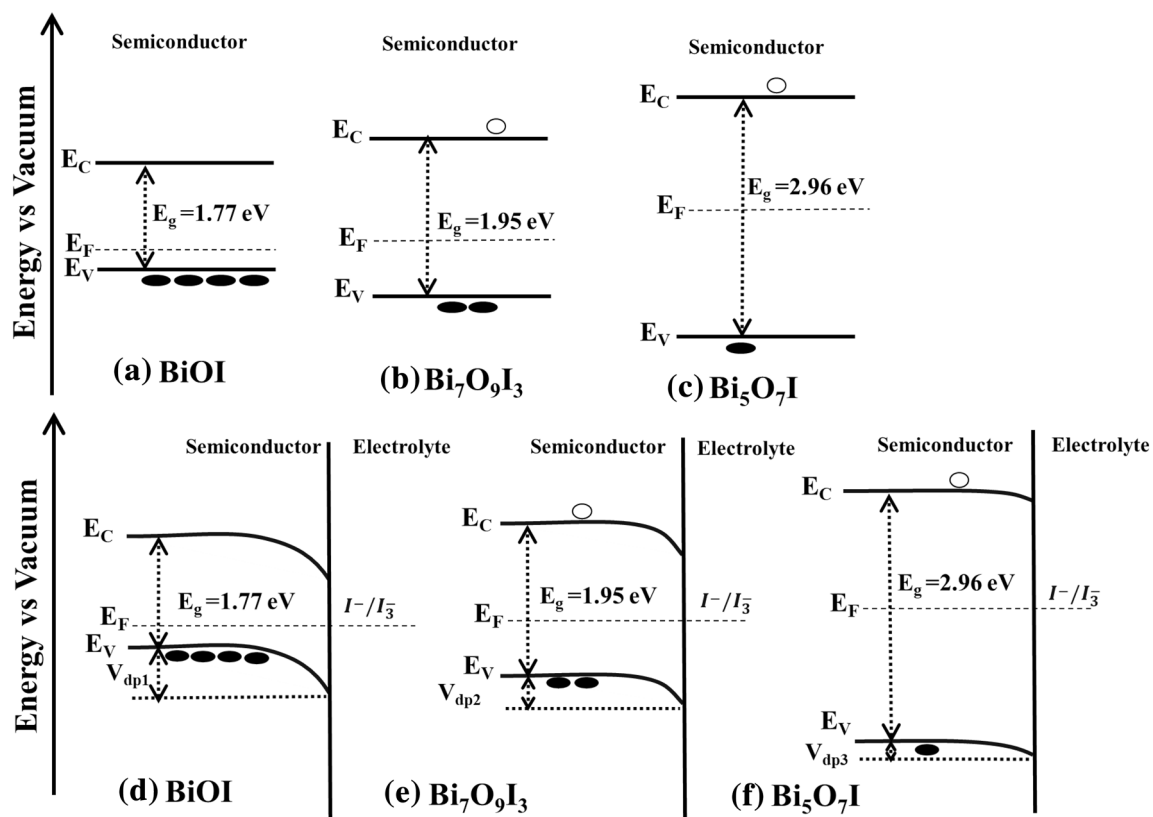


Fig. 12 Illustration of energy band diagram: without the contact of electrolyte **a, b, c** and with the contact of electrolyte **d, e, f**

4 Conclusion

The effect of phase transformation on photovoltaic characteristics of bismuth oxyhalides films has been investigated. The experimental results show that for dip-SILAR-prepared BiOI photovoltaic solar cell after phase transformation from BiOI to Bi₇O₉I₃ and Bi₅O₇I, the electrical properties are getting worse. This was due to that variation of annealing temperature changes the films' structural, morphological, and optical properties, resulting in the change of energy band diagram with electrolyte. BiOI film's crystallinity without annealing is poor but is increased via crystallization by annealing at 100 °C. But further increase of annealing temperature causes desorption of iodine, resulting in the poor crystallinity and photovoltaic performance. We observed phase transformation was started after 200 °C annealing temperature, and Bi₇O₉I₃ is confirmed at 300 °C. Moreover, we got the Bi₅O₇I phase at 400 °C. Again, with the increase in annealing temperature, the band-gap increases from 1.77 to 2.96 eV, and the crystallite size decreases from 17.62 to 12.99 nm. At 100 °C, we found maximum J_{sc} , V_{oc} and efficiency, which is 0.6 mA/cm², 0.43 V, and 0.11% respectively, and at 400 °C, we observed the minimum J_{sc} , V_{oc} and efficiency, which is 0.01 mA/cm², 0.04 V and 0.0001%, respectively. Finally, we can conclude that the optimal annealing temperature for dip-SILAR-prepared BiOI/FTO photovoltaic cells is 100 °C.

Compliance with ethical standards

Conflict of Interest The authors declare that there is no conflict of interest regarding the publication of this article.

Open Access This article is licensed under a Creative Commons Attribution 4.0 International License, which permits use, sharing, adaptation, distribution and reproduction in any medium or format, as long as you give appropriate credit to the original author(s) and the source, provide a link to the Creative Commons licence, and indicate if changes were made. The images or other third party material in this article are included in the article's Creative Commons licence, unless indicated otherwise in a credit line to the material. If material is not included in the article's Creative Commons licence and your intended use is not permitted by statutory regulation or exceeds the permitted use, you will need to obtain permission directly from the copyright holder. To view a copy of this licence, visit <http://creativecommons.org/licenses/by/4.0/>.

References

- Lee WW, Lu CS, Chuang CW, Chen YJ, Fu JY, Siao CW, Chen CC (2015) Synthesis of bismuth oxyiodides and their composites: characterization, photocatalytic activity, and degradation mechanisms. *RSC Adv* 5(30):23450–23463
- He R, Zhang J, Yu J, Cao S (2016) Room-temperature synthesis of BiOI with tailorable (0 0 1) facets and enhanced photocatalytic activity. *J Colloid Interface Sci* 478:201–208
- Zhang X, Zhang L (2010) Electronic and band structure tuning of ternary semiconductor photocatalysts by self-doping: the case of BiOI. *J Phys Chem C* 114(42):18198–18206
- Niu J, Dai P, Zhang Q, Yao B, Yu X (2018) Microwave-assisted solvothermal synthesis of novel hierarchical BiOI/rGO composites for efficient photocatalytic degradation of organic pollutants. *Appl Surf Sci* 430:165–175
- Zhang X, Zhang L, Xie T, Wang D (2009) Low-temperature synthesis and high visible-light-induced photocatalytic activity of BiOI/TiO₂ heterostructures. *J Phys Chem C* 113(17):7371–7378
- Cao J, Xu B, Luo B, Lin H, Chen S (2011) Novel BiOI/BiOBr heterojunction photocatalysts with enhanced visible light photocatalytic properties. *Catal Commun* 13(1):63–68
- Hou J, Jiang K, Shen M, Wei R, Wu X, Idrees F, Cao C (2017) Micro and nano hierarchical structures of BiOI/activated carbon for efficient visible-light-photocatalytic reactions. *Sci Rep* 7(1):1–10
- Hao R, Xiao X, Zuo X, Nan J, Zhang W (2012) Efficient adsorption and visible-light photocatalytic degradation of tetracycline hydrochloride using mesoporous BiOI microspheres. *J Hazard Mater* 209:137–145
- Cheng H, Huang B, Dai Y, Qin X, Zhang X (2010) One-step synthesis of the nanostructured AgI/BiOI composites with highly enhanced visible-light photocatalytic performances. *Langmuir* 26(9):6618–6624
- Han A, Zhang H, Chuah GK, Jaenicke S (2017) Influence of the halide and exposed facets on the visible-light photoactivity of bismuth oxyhalides for selective aerobic oxidation of primary amines. *Appl Catal B Environ* 219:269–275
- Hoye RL, Lee LC, Kurchin RC et al (2017) Strongly enhanced photovoltaic performance and defect physics of air-stable bismuth oxyiodide (BiOI). *Adv Mater* 29(36):1702176
- Wang L, Daoud WA (2015) BiOI/TiO₂-nanorod array heterojunction solar cell: growth, charge transport kinetics and photoelectrochemical properties. *Appl Surf Sci* 324:532–537
- Sfaelou S, Raptis D, Dracopoulos V, Lianos P (2015) BiOI solar cells. *RSC Adv* 5(116):95813–95816
- Zhang Y, Pei Q, Liang J et al (2015) Mesoporous TiO₂-based photoanode sensitized by BiOI and investigation of its photovoltaic behavior. *Langmuir* 31(37):10279–10284
- Wang K, Jia F, Zhang L (2013) Facile construction of low-cost flexible solar cells with p-type BiOI nanoflake arrays fabricated via oriented attachment. *Mater Lett* 92:354–357
- Wang K, Jia F, Zheng Z, Zhang L (2010) Crossed BiOI flake array solar cells. *Electrochem Commun* 12(12):1764–1767
- Zhang Y, Li Y, Sun W, Yuan C, Wang B, Zhang W, Song XM (2017) Fe₂O₃/BiOI-based photoanode with np heterogeneous structure for photoelectric conversion. *Langmuir* 33(43):12065–12071
- Lei Y, Wang G, Song S, Fan W, Pang M, Tang J, Zhang H (2010) Room temperature, template-free synthesis of BiOI hierarchical structures: visible-light photocatalytic and electrochemical hydrogen storage properties. *Dalton Trans* 39(13):3273–3278
- Xiao X, Zhang WD (2010) Facile synthesis of nanostructured BiOI microspheres with high visible light-induced photocatalytic activity. *J Mater Chem* 20(28):5866–5870
- Long Y, Han Q, Yang Z et al (2018) A novel solvent-free strategy for the synthesis of bismuth oxyhalides. *J Mater Chem A* 6(27):13005–13011
- Putri AA, Kato S, Kishi N, Soga T (2019) Study of annealing temperature effect on the photovoltaic performance of BiOI-based materials. *Appl Sci* 9(16):3342
- Meledandri CJ, Stolarczyk JK, Ghosh S, Brougham DF (2008) Non-aqueous magnetic nanoparticle suspensions with controlled

- particle size and nuclear magnetic resonance properties. *Langmuir* 24(24):14159–14165
23. Demortiere A, Panissod P, Pichon BP, Pourroy G, Guillon D, Donnio B, Begin-Colin S (2011) Size-dependent properties of magnetic iron oxide nanocrystals. *Nanoscale* 3(1):225–232
 24. Effenberger FB, Couto RA, Kiyohara PK, Machado G, Masunaga SH, Jardim RF, Rossi LM (2017) Economically attractive route for the preparation of high quality magnetic nanoparticles by the thermal decomposition of iron (III) acetylacetonate. *Nanotechnology* 28(11):115603
 25. Hufschmid R, Arami H, Ferguson RM et al (2015) Synthesis of phase-pure and monodisperse iron oxide nanoparticles by thermal decomposition. *Nanoscale* 7(25):11142–11154
 26. Baaziz W, Pichon BP, Fleutot S et al (2014) Magnetic iron oxide nanoparticles: reproducible tuning of the size and nanosized-dependent composition, defects, and spin canting. *J Phys Chem C* 118(7):3795–3810
 27. Long M, Hu P, Wu H, Chen Y, Tan B, Cai W (2015) Understanding the composition and electronic structure dependent photocatalytic performance of bismuth oxyiodides. *J Mater Chem A* 3(10):5592–5598
 28. Xiao X, Liu C, Hu R, Zuo X, Nan J, Li L, Wang L (2012) Oxygen-rich bismuth oxyhalides: generalized one-pot synthesis, band structures and visible-light photocatalytic properties. *J Mater Chem* 22(43):22840–22843
 29. Xia J, Ji M, Di J, Wang B et al (2017) Improved photocatalytic activity of few-layer $\text{Bi}_4\text{O}_5\text{I}_2$ nanosheets induced by efficient charge separation and lower valence position. *J Alloys Compd* 695:922–930
 30. Xiao X, Zhang WD (2011) Hierarchical $\text{Bi}_7\text{O}_9\text{I}_3$ micro/nano-architecture: facile synthesis, growth mechanism, and high visible light photocatalytic performance. *RSC Adv* 1(6):1099–1105
 31. Yang J, Xu L, Liu C, Xie T (2014) Preparation and photocatalytic activity of porous $\text{Bi}_5\text{O}_7\text{I}$ nanosheets. *Appl Surf Sci* 319:265–271
 32. Abuelwafa AA, Matiur RM, Putri AA, Soga T (2020) Synthesis, structure, and optical properties of the nanocrystalline bismuth oxyiodide (BiOI) for optoelectronic application. *Opt Mater* 109:110413
 33. Matiur RM, Abuelwafa AA, Kato S, Kishi N, Soga T (2020) A comparative study on optical properties of BiOI , $\text{Bi}_7\text{O}_9\text{I}_3$ and $\text{Bi}_5\text{O}_7\text{I}$ materials. *Opt Mater*. <https://doi.org/10.1016/j.optmat.2020.110677>
 34. Mera AC, Rodríguez CA, Meléndrez MF, Valdés H (2017) Synthesis and characterization of BiOI microspheres under standardized conditions. *J Mater Sci* 52(2):944–954
 35. Yang R, Li H, Wang Y, Zhu Z et al (2020) A novel flower-like Z-type heterojunction $\text{CuS}/\text{Bi}_7\text{O}_9\text{I}_3$ composite catalyst prepared under mild conditions for degradation of antibiotics and sterilization under visible light. *Environ Sci Nano* 7(10):3074–3087
 36. Sun S, Wang W, Zhang L, Zhou L, Yin W, Shang M (2009) Visible light-induced efficient contaminant removal by $\text{Bi}_5\text{O}_7\text{I}$. *Environ Sci Technol* 43(6):2005–2010
 37. Hassanien AS, Akl AA, SÁaedi AH (2018) Synthesis, crystallography, microstructure, crystal defects, and morphology of $\text{Bi}_x\text{Zn}_{1-x}\text{O}$ nanoparticles prepared by sol–gel technique. *CrystEngComm* 20(12):1716–1730
 38. Romero R, Leinen D, Dalchiale EA, Ramos-Barrado JR, Martín F (2006) The effects of zinc acetate and zinc chloride precursors on the preferred crystalline orientation of ZnO and Al-doped ZnO thin films obtained by spray pyrolysis. *Thin Solid Films* 515(4):1942–1949
 39. Abuelwafa AA, Abd El-sadek MS, Yahia IS (2018) Linear and non-linear optical properties of nano-spherical Perylenetetracarboxylic dianhydride/ITO as a new optical system. *Opt Laser Technol* 108:241–246
 40. Bayansal F, Şahin B, Yüksel M, Biyikli N, Çetinkara HA, Güder HS (2013) Influence of coumarin as an additive on CuO nanostructures prepared by successive ionic layer adsorption and reaction (SILAR) method. *J Alloys Compd* 566:78–82
 41. Das MR, Roy A, Mpelane S, Mukherjee A, Mitra P, Das S (2018) Influence of dipping cycle on SILAR synthesized NiO thin film for improved electrochemical performance. *Electrochim Acta* 273:105–114
 42. Abuelwafa AA, El-Denglawey A, Dongol M, El-Nahass MM, Soga T (2016) Structural and optical properties of nanocrystalline platinum octaethylporphyrin (PTOEP) thin films. *J Alloys Compd* 655:415–422
 43. Putri AA, Abuelwafa AA, Kato S, Kishi N, Soga T (2020) A simple spin-assisted SILAR of bismuth oxyiodide films preparation for photovoltaic application. *SN Appl Sci* 2(1):119
 44. Gopalakrishna D, Vijayalakshmi K, Ravidhas C (2013) Effect of annealing on the properties of nanostructured CuO thin films for enhanced ethanol sensitivity. *Ceram Int* 39(7):7685–7691
 45. Sahin B, Bayansal F, Çakmak HM, Kahraman S, Çetinkara HA (2013) Effect of heat treatment on the properties of $\text{Cd}(\text{OH})_2$ and CdO films grown by chemical bath deposition. *Philos Mag Lett* 93(2):101–108
 46. Roknuzzaman M, Alarco JA, Wang H, Ostrikov KK (2021) Structural, electronic and optical properties of lead-free antimony-copper based hybrid double perovskites for photovoltaics and optoelectronics by first principles calculations. *Comput Mater Sci* 186:110009
 47. Roknuzzaman M, Ostrikov KK, Wasalathilake KC, Yan C, Wang H, Tesfamichael T (2018) Insight into lead-free organic-inorganic hybrid perovskites for photovoltaics and optoelectronics: a first-principles study. *Org Electron* 59:99–106
 48. Fang M, Jia H, He W, Lei Y, Zhang L, Zheng Z (2015) Construction of flexible photoelectrochemical solar cells based on ordered nanostructural $\text{BiOI}/\text{Bi}_2\text{S}_3$ heterojunction films. *Phys Chem Chem Phys* 17(20):13531–13538
 49. Arumugam M, Choi MY (2020) Recent progress on bismuth oxyiodide (BiOI) photocatalyst for environmental remediation. *J Ind Eng Chem* 81:237–268
 50. Mendoza Herrera LJ, Arboleda DM, Schinca DC, Scaffardi LB (2014) Determination of plasma frequency, damping constant, and size distribution from the complex dielectric function of noble metal nanoparticles. *J Appl Phys* 116(23):233105
 51. Dongol M, Elhady AF, Ebied MS, Abuelwafa AA (2018) Impact of sulfur content on structural and optical properties of $\text{Ge}_{20}\text{Se}_{80-x}\text{S}_x$ chalcogenide glasses thin films. *Opt Mater* 78:266–272
 52. Dongol M, Elhady AF, Ebied MS, Abuelwafa AA (2020) Effect of thermal annealing on the optical properties of $\text{Ge}_{20}\text{Se}_{65}\text{S}_{15}$ thin films. *Indian J Phys*. <https://doi.org/10.1007/s12648-020-01787-3>
 53. Xu W, Fang J, Zhu X, Fang Z, Cen C (2015) Fabrication of improved novel p–n junction $\text{BiOI}/\text{Bi}_2\text{Sn}_2\text{O}_7$ nanocomposite for visible light driven photocatalysis. *Mater Res Bull* 72:229–234
 54. Liu C, Wang XJ (2016) Room temperature synthesis of $\text{Bi}_4\text{O}_5\text{I}_2$ and $\text{Bi}_5\text{O}_7\text{I}$ ultrathin nanosheets with a high visible light photocatalytic performance. *Dalton Trans* 45(18):7720–7727
 55. Lin J, Hu Z, Li H, Qu J, Zhang M, Liang W, Hu S (2019) Ultrathin nanotubes of $\text{Bi}_5\text{O}_7\text{I}$ with a reduced band gap as a high-performance Photocatalyst. *Inorg Chem* 58(15):9833–9843

Publisher's Note Springer Nature remains neutral with regard to jurisdictional claims in published maps and institutional affiliations.